PCCP

PAPER

View Article Online
View Journal | View Issue

Cite this: *Phys. Chem. Chem. Phys.*, 2018, **20**, 20661

Phosphomolybdic acid supported single-metal-atom catalysis in CO oxidation: first-principles calculations†

Ming-an Yu, Yingxin Feng, Liye Gao and Sen Lin *

Received 20th June 2018,
Accepted 18th July 2018

DOI: 10.1039/c8cp03916j

rsc.li/pccp

CO oxidation on phosphomolybdic acid ($H_3PMo_{12}O_{40}$, PMA) supported single-metal atom (M = Pt, Au, Co, Cu, Fe, Ir, Ni, Os, Pd, Ag, Rh, and Ru) (M-PMA) catalysts is studied by density-functional-theory (DFT) calculations. Adsorption of CO and O_2 on M-PMA is investigated. Based on electronic structure analysis, O_2 is activated by the single-metal-atom active center. The Langmuir–Hinshelwood mechanism is systematically explored for CO oxidation on M-PMA, and it is found that M-PMAs have high reactivity toward CO oxidation. The Mars–van Krevelen mechanism is also investigated and it is shown to be less likely to be responsible. Our DFT findings will provide useful insight for designing stable, highly active heteropolyacid-supported single-metal-atom catalysts.

1. Introduction

Catalytic CO oxidation has attracted increasing interest because of its great importance in solving the growing environmental problems caused by CO emission.[1–12] Selective oxidation of CO is also known as a key step in fuel cell applications for eliminating CO from reforming gas.[13] Moreover, the conversion of CO to CO_2 is an important step in the water gas shift reaction.[14] Although previous studies have shown that some noble metals, such as Au and Pt, can effectively catalyze CO oxidation,[15–19] their implementation is significantly hindered by the high costs of noble metals. Therefore, reducing the amount of metals used during CO oxidation catalysis remains as a challenge.

Single-atom catalysts (SACs) supported on various substrates have attracted special attention due to their intrinsic high activity, efficiency, stability, and low cost.[20–25] The atomic form of the catalyst greatly increases the catalytic efficiency, which could potentially lead to a dramatic reduction in the quantity and cost of precious metals required. For example, Nie *et al.* showed that atomically dispersed Pt^{2+} on CeO_2 was thermally stable and possesses high activity for CO oxidation at 150 °C.[26] In another report, Zhang's group found that Pt atoms were able to atomically disperse on the surfaces of iron oxide (FeO_x) with high stability and high activity for CO oxidation.[27] Stability is a key concern for SACs because they usually form nanoparticles through agglomeration at high temperatures, resulting in a significant loss of reaction activity.[28] Therefore, the development of new supports that strongly bind metal atoms remains a challenge in the design of stable SACs.

Heteropolyacids, such as phosphomolybdic acid ($H_3PMo_{12}O_{40}$, PMA) and phosphotungstic acid ($H_3PW_{12}O_{40}$, PTA), have emerged as a superior support for single atoms to be stably anchored because of their particular structure, which has a range of coordination sites containing exposed O atoms.[29] Zhang *et al.* first developed single Pt atoms supported on PMA.[29,31] Of particular note, they found that Pt atoms adsorb strongly at the fourfold hollow site on PMA. The results of subsequent catalysis tests show that these supported Pt atoms exhibit high activity for hydrogenation reactions with high selectivity. Additional recent density-functional-theory (DFT) work indicates that 12 different transition metal atoms (Fe, Co, Ni, Cu, Ru, Rh, Pd, Ag, Os, Ir, Pt, and Au) supported by PMA have very high stability, with binding energies of transition metals higher than those on widely used metal oxide supports, suggesting that they are sufficiently stable to prevent agglomeration.[32]

Recently, Zhang *et al.* reported that Rh atoms can be atomically dispersed on PTA, with Rh loading up to 0.9 wt% and high activity for CO oxidation.[30] This result opens several new directions for designing stable heterogeneous SACs for CO oxidation. Two research areas are of particular interest for the present study. First, given that PTA-supported Rh SACs have high activity for CO oxidation, it is natural to ask whether metal atoms supported on PMA have the same performance. Second, it is desirable to know the more likely reaction mechanism for CO oxidation on PMA-supported metal atoms: the Langmuir–Hinshelwood (LH) mechanism or the Mars–van Krevelen (MvK) mechanism.

State Key Laboratory of Photocatalysis on Energy and Environment, College of Chemistry, Fuzhou University, Fuzhou 350002, China. E-mail: slin@fzu.edu.cn

† Electronic supplementary information (ESI) available. See DOI: 10.1039/c8cp03916j

In the present work, we investigate CO oxidation catalyzed by M-PMA (M = Fe, Ag, Ni, Co, Cu, Ir, Ni, Os, Pd, Pt, Rh, or Ru) using DFT methods. Adsorption of CO and O_2 on M-PMA is investigated. Reaction mechanisms are systematically explored for CO oxidation on M-PMA. This publication is organized as follows. The calculation details are described in Section 2. The Results and discussion are presented in Section 3. The conclusions are given in Section 4.

2. Computational details

All spin-polarization calculations were carried out using the Vienna *Ab initio* Simulation Package[33–37] (VASP) with the gradient-corrected PW91 exchange-correction functional.[38] For valence electrons, a plane-wave basis set was used with the energy cutoff set to 400 eV, and the ionic cores were described with the projector augmented-wave (PAW) method.[39,40] A cubic unit cell with a side length of 20 Å contains a PMA molecule with an added metal atom. For structural optimizations, all the atoms were fully relaxed and only the Γ point was used to sample the Brillouin zone.[41] The electron density for the ground state was converged with a 10^{-4} eV total energy threshold, and the geometries were optimized until the maximum force on any ion was less than 0.05 eV $Å^{-1}$.

The adsorption energy E_{ads} was defined as $E_{ads} = E_{(adsorbate+catalyst)} - E_{(adsorbate)} - E_{(catalyst)}$, where $E_{(adsorbate+catalyst)}$ is the total energy of the adsorbate interacting with the catalyst and $E_{(adsorbate)}$ and $E_{(catalyst)}$ are, respectively, the energies of the free adsorbate and the pure catalyst. The climbing image nudged elastic band[42] (CI-NEB) method was adopted to simulate CO oxidation on heteropolyacid-supported single-metal atoms. The activation barrier E_a for the reaction was calculated by the energy difference between the transition state (TS) and the initial state (IS), while the reaction energy ΔE for each reaction step was calculated by the energy difference between the final state (FS) and the IS. Vibrational analyses were further performed to ensure the stationary point characteristics of the local minima and transition states. The DFT-D3 method of Grimme was performed to obtain the energy barriers of CO oxidation on Pt-PMA and Ru-PMA. The test results indicate that the differences between the values with and without dispersion correction are smaller than 0.04 eV. Therefore, the dispersion correction plays a minor role in our system and thus is not included in this work.

3. Results and discussion

3.1 Adsorption of CO and O_2 on M-PMA

In this work, PMA was selected as a model of a heteropolyacid support. As shown in Fig. 1, PMA has a classical Keggin structure consisting of Mo and O atoms with a P atom located in the center. All possible adsorption sites on PMA including a 4-fold hollow site (4-H), two 3-fold hollow sites (3H–O_c and 3H–O_{bri}) and a bridge site (B–O_c–O_{bri}) are also displayed in Fig. 1. Our previous work indicated that transition metals (Pt, Au, Co, Cu, Fe, Ir, Ni, Os, Pd, Ag, Rh, or Ru) prefer to locate at the 4-H site on PMA in a distorted square-planar geometry.[32]

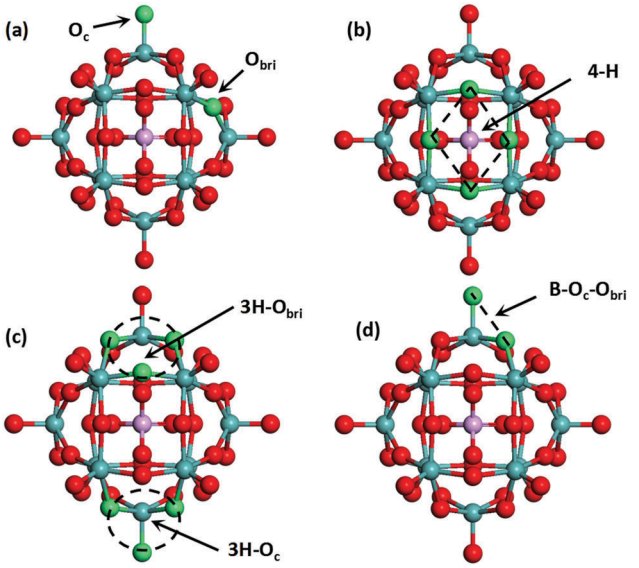

Fig. 1 Optimized geometries of PMA. Color scheme: P, pink; O, red; and Mo, green.

To gain a better understanding of the interaction between the trapped metal atoms and 4-H of PMA, the spin-polarized local densities of states (LDOSs) projected onto the M-3d and neighboring O-2p orbitals are computed. From the LDOSs plotted in Fig. S1 (ESI†), it is clear to see that the 3d orbitals of the M atom are strongly coupled with the 2p orbitals of the O atoms at 4-H sites above and below the Fermi level (E_F). The results suggest a strong interaction between M and PMA and M is stable on PMA.

Before exploring CO oxidation, the adsorption of CO and O_2 on M-PMA was systematically investigated. The optimized adsorption structures for these two species are displayed in Fig. 2 and 3, and the adsorption energies and structural parameters are listed in Table 1. CO absorption on M-PMA occurs with the C end facing the metal site at a titled angle. As stated in Table 1, CO binds most weakly on Cu-PMA, with an E_{ads} of only −0.14 eV and a distance of 2.42 Å between the C and Cu atoms. The strongest interaction is found on Ir-PMA, with an adsorption energy of −2.25 eV. The calculated C–O distances of CO adsorption on M-PMA are in the range 1.14 to 1.18 Å, equal or close to that (1.14 Å) of an isolated CO molecule. It can be seen that CO binds too strongly on Pt-PMA, Ir-PMA, and Ru-PMA, which might lead to the poisoning of catalysts. A deeper understanding of the actual CO-poisoning on these catalysts can be obtained by further experiments. Furthermore, we notice that some of the calculated binding energies of CO on PMA supported metal atoms are significantly different from those for CO adsorption on free standing small clusters (*e.g.* M_2 or M_4, M = Ni, Cu, Ru, Rh, Pd, Ag, Ir, Pt and Au).[43] For example, the adsorption energy of CO on Ni-PMA is −0.58 eV, while the values (−1.43 and −2.15 eV) are much larger on Ni_2 and Ni_4, respectively;[43] on Rh-PMA, the binding energy of CO (−0.45 eV) is much smaller than −1.58 eV on Rh_2 and −1.61 eV on Rh_4.[43] Such a difference might be attributed to the fact that the PMA support modifies the electronic structures of metals.

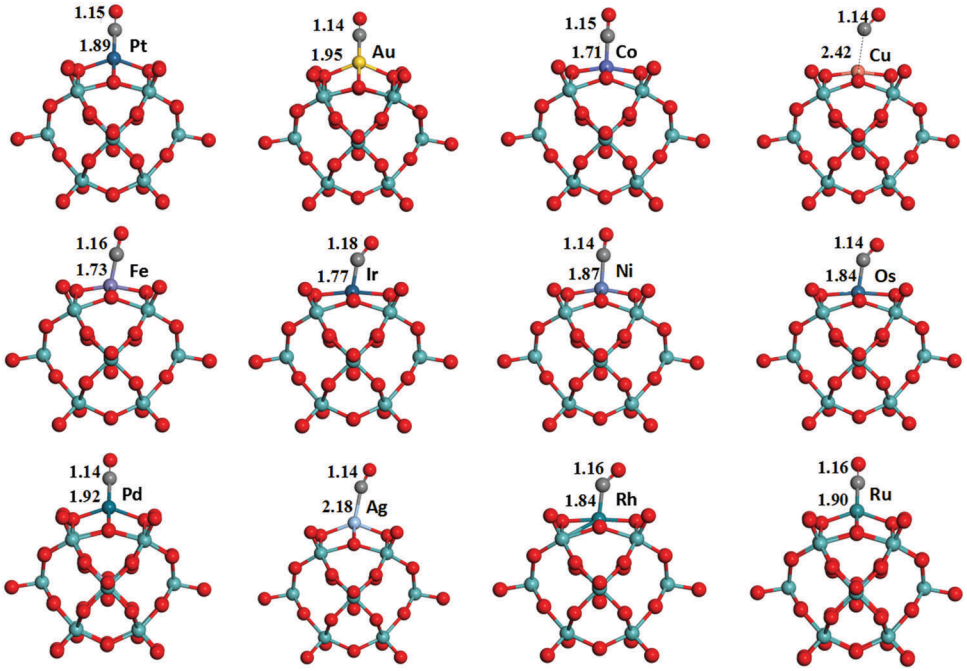

Fig. 2 Most stable structures of CO adsorbed on M-PMA.

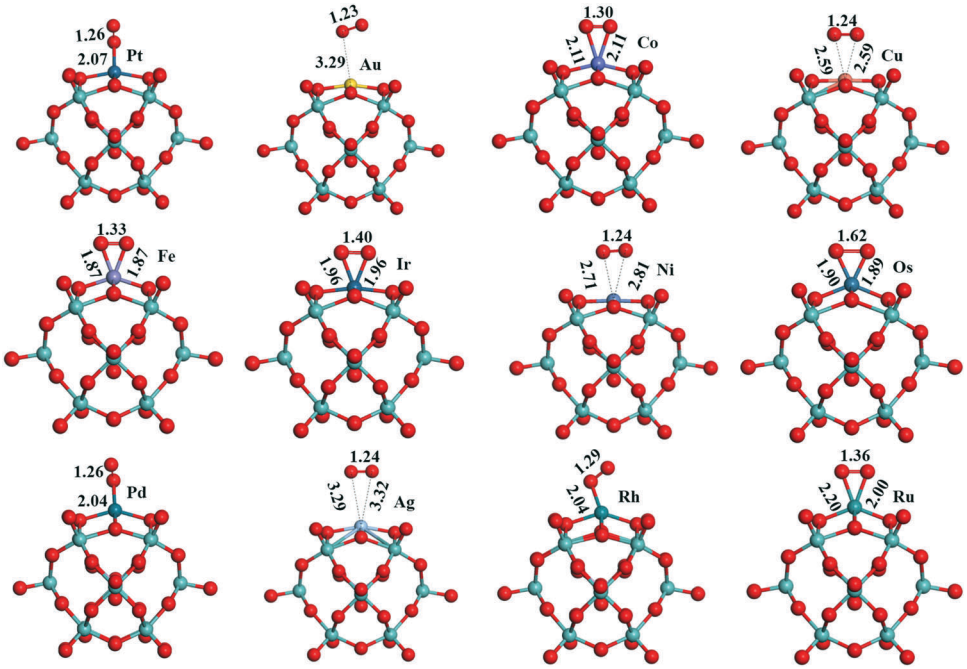

Fig. 3 Most stable structures of O_2 adsorbed on M-PMA.

For O_2 adsorption on M-PMA, different configurations are observed for different metal atoms. The adsorption of O_2 is very weak on Au-PMA, Co-PMA, Cu-PMA, and Ni-PMA, with calculated binding energies of (respectively) −0.03, 0.09, 0.29, and 0.18 eV and distances of more than 2.50 Å between the metal atom and the O_2 adsorbate. For Pt-PMA, Fe-PMA, Ir-PMA, Os-PMA, Pd-PMA, Rh-PMA, and Ru-PMA, the calculated binding energies are −1.54, −0.48, −0.99, −0.82, −0.46, −0.44, and −1.37 eV, respectively. We find that O_2 prefers to lie parallel over the Fe, Ir, Os, and Ru metal sites with both two O atoms connecting to the metal atom, while for Pt, Pd, and Rh only one O atom in O_2 connects with the metal atom. It can be seen from Table 1 that the bond lengths of the adsorbed O_2 are elongated from 1.23 Å to lengths in the range 1.26–1.62 Å, indicating that the adsorbed O_2 molecule is activated by the single-metal center.

Table 1 Calculated adsorption energies of CO and O_2, distances between CO/O_2 and M-PMA, and bond lengths of adsorbed CO and O_2 on M-PMA

	Pt-PMA	Au-PMA	Co-PMA	Cu-PMA	Fe-PMA	Ir-PMA
			CO			
E_{ad}	−1.54	−0.80	−0.86	−0.14	−0.54	−2.25
d_{C-O} (Å)	1.15	1.14	1.15	1.14	1.16	1.18
d_{M-C} (Å)	1.89	1.95	1.71	2.42	1.73	1.77
			O_2			
E_{ad}	−0.44	−0.03	0.09	0.29	−0.48	−0.99
d_{O-O} (Å)	1.26	1.23	1.30	1.24	1.33	1.40
d_{M-O} (Å)	2.07	3.29	2.11	2.59	1.87	1.96
	Ni-PMA	Os-PMA	Pd-PMA	Ag-PMA	Rh-PMA	Ru-PMA
			CO			
E_{ad}	−0.58	−0.32	−0.83	−0.32	−0.45	−1.92
d_{C-O} (Å)	1.14	1.14	1.14	1.14	1.16	1.16
d_{M-C} (Å)	1.87	1.84	1.95	2.18	1.84	1.90
			O_2			
E_{ad}	0.18	−0.82	−0.46	−0.01	−0.44	−1.37
d_{O-O} (Å)	1.24	1.62	1.26	1.24	1.29	1.36
d_{M-O} (Å)	2.71	1.89	2.04	3.29	2.04	2.00

One may ask whether M-PMA can remain stable upon adsorption of CO or O_2. The calculated structural parameters including d_{O-M} and ∠O–M–O are listed in Table S2 (ESI†). Obviously, these M-PMA structures are slightly changed upon adsorption of CO or CO.

Since the activation of O_2 is known as one of the most important steps in CO oxidation, the electronic structures of the adsorbed O_2 molecules on M-PMA were analyzed to better understand the interaction between O_2 and M-PMA. As evidenced by the local density of states (LDOS) in Fig. 4, there is strong coupling between the 2p orbitals of O_2 and the 3d orbitals of the metal. This coupling leads to electron transfer from the M-PMA catalyst to occupy the $2\pi^*$ orbitals of O_2*, resulting in the elongation of the O–O bond of O_2.

3.2 Mechanism of CO oxidation on M-PMA

Weak interactions between O_2 and Au, Co, Cu, Ag, or Ni suggest that these metals cannot activate the O_2 molecule. The remaining metals (Pt, Fe, Ir, Os, Pd, Rh, and Ru) were able to activate O_2 and might catalyze CO oxidation. In this work, only five M-PMAs (M = Pt, Fe, Ir, Rh, or Ru) were selected for further study as model CO oxidation catalysts due to the significant computational expense of the CI-NEB calculations required to locate transition states. The entire catalytic cycle of CO oxidation on M-PMA is composed of two reaction steps, namely the oxidation [reaction (R1)] between the first CO and O_2 that leads to CO_2 and a residual O, and the subsequent oxidation [reaction (R2)] between the second CO and the residual O which generates a second CO_2:

$$CO + O_2 \rightarrow CO_2 + O \quad (R1)$$

$$CO + O \rightarrow CO_2 \quad (R2)$$

In previous studies, two mechanisms for CO oxidation were proposed: the LH mechanism and the Eley–Rideal (ER) mechanism.[44] For the LH mechanism, O_2 and CO co-adsorb on M-PMA before the reaction, while for the ER mechanism the pre-adsorbed O_2 molecule is activated by M-PMA first and a free CO molecule approaches to react with O_2. Because the adsorption energies of CO on M-PMA are larger than those for O_2, it is more likely that CO will be found adsorbed rather than as a free gas molecule. This makes the ER mechanism less probable than the LH pathway, and in the following section the ER mechanism is not investigated.

The calculated energy barriers and reaction energies are given in Table 2. Here, Pt-PMA is taken as an example to trace the entire reaction path of CO oxidation (the structural parameters for the other M-PMAs are given in Table S1 of the ESI†). Diagrams for CO oxidation following the LH reaction mechanism on Pt-PPM are shown in Fig. 5. For (R1), the co-adsorption of CO and O_2 on

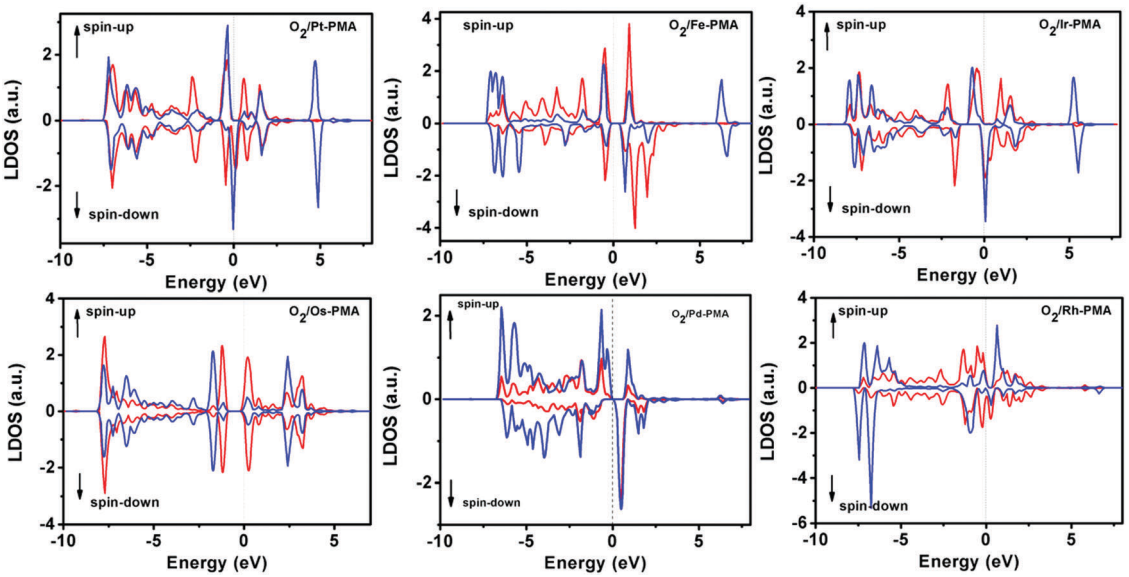

Fig. 4 Corresponding spin-polarized LDOSs of O_2 adsorption on M-PMA (M = Pt, Fe, Ir, Os, Pd, and Rh). Red and blue curves denote d orbitals of metals and p orbitals of O_2, respectively. The Fermi level is set to 0 eV.

Table 2 Reaction barriers E_a and ΔE for CO oxidation following the LH mechanism on M-PMA (M = Pt, Fe, Ir, Rh, and Ru)

M	Reaction	E_a	ΔE
Pt	$CO + O_2 \rightarrow CO_2 + O$	0.59	−1.01
	$CO + O \rightarrow CO_2$	0.22	−2.13
Fe	$CO + O_2 \rightarrow CO_2 + O$	0.56	−3.36
	$CO + O \rightarrow CO_2$	0.41	−2.67
Ir	$CO + O_2 \rightarrow CO_2 + O$	0.86	−1.79
	$CO + O \rightarrow CO_2$	0.87	−0.37
Rh	$CO + O_2 \rightarrow CO_2 + O$	0.87	−1.67
	$CO + O \rightarrow CO_2$	0.61	−1.50
Ru	$CO + O_2 \rightarrow CO_2 + O$	0.75	−3.13
	$CO + O \rightarrow CO_2$	0.07	−0.22

the single Pt site is considered the initial state (state i). The O–O bond length of O_2 is elongated to 1.27 Å from its gaseous state. The distances between the Pt atom and the two O atoms of O_2 species are approximately 2.10 and 2.88 Å, respectively, and the Pt–C bond length is 1.91 Å. In the transition state (TS1), we can see that the distance between C and the O atom of O_2 is 1.69 Å and the O–O bond length is elongated to 1.37 Å. The energy barrier is calculated to be 0.59 eV and the reaction is exothermic (−1.01 eV). Next, a CO_2 (state iii) molecule is produced with a small binding energy of 0.12 eV near the residual O atom. For R2, CO and O are co-adsorbed in the initial state (state iv) with the distance between the C atom and the O atom equal to 1.14 Å. In the transition state (TS2), it can be seen that a bent CO_2 molecule is nearly formed with a C–Pt distance of 2.29 Å. This reaction should overcome an energy barrier of 0.22 eV with an exothermicity of −2.13 eV. Finally, a second CO_2 molecule is produced and the catalyst is recovered. The barrier (0.59 eV) of the rate-determining step is almost equal to that (<0.60 eV) on $Pt_1@CeO_2(111)$ and $Pt_1@CeO_2(100)$,[45] and much lower than those (0.87 and 0.79 eV, respectively) on $Pt_1@CeO_2(110)$ and $Pt_1/CeO_2(110)$.[45,46] In addition, Pt-PMA seems more active for CO oxidation than Pt_1/FeO_x on which a larger energy barrier (0.79 eV) is found.[20] Therefore, Pt-PMA has high activity for CO oxidation at low temperatures. The calculated barriers of R1 on M-PMA (M = Fe, Ir, Rh, and Ru) are 0.56, 0.97, 0.87, and 0.75 eV, respectively, with respective exothermicities of −3.36, −1.79, −1.67, and −3.13 eV. For R2, the energy barriers are found to be 0.41, 0.59, 0.61, and 0.07 eV on Fe, Ir, Rh, and Ru supported on PMA, respectively. The calculated reaction energies (as shown in Table 2) also indicate that R2 on these M-PMAs is thermally favored. It would be interesting to compare the CO oxidation activity of M-PMA with the single metal atoms on other widely used supports such as Al_2O_3, CeO_2 and FeO_x. For Fe-PMA, the activity of CO oxidation is much higher than that for Fe_1/Al_2O_3 on which a large energy barrier of 1.49 eV should be overcome.[47] In particular, the low energy barrier (0.56 eV) also suggests that Fe-PMA might be a potential non-noble-metal catalyst. For the single Ir atom, we found that the energy barrier for the rate-determining step of CO oxidation on Ir_1/FeO_x is as high as 1.41 eV,[10] significantly larger than that (0.97 eV) on Ir-PMA.

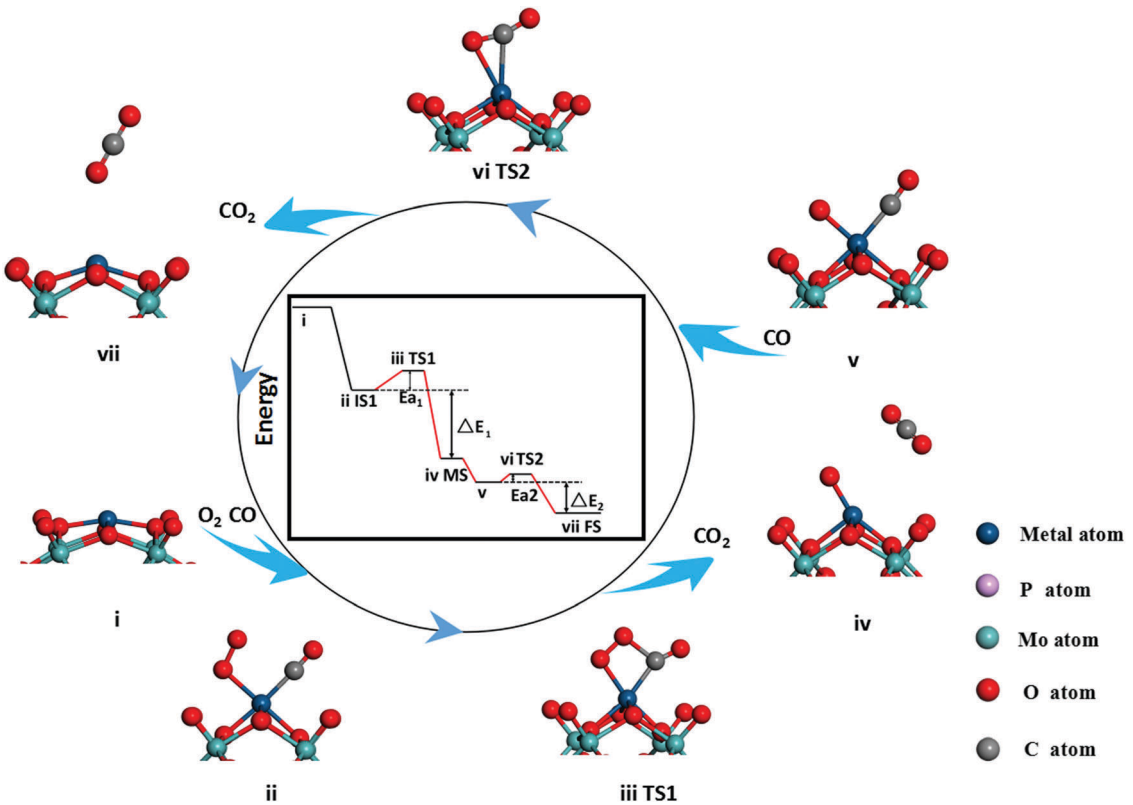

Fig. 5 Diagrams for CO oxidation following the LH reaction mechanism on M-PMA (M = Pt). (i) M-PMA catalyst, (ii) co-adsorption of CO and O_2 on the metal site, (iii) the transition state (TS1) for $CO + O_2 \rightarrow CO_2 + O$, (iv) the first produced CO_2 molecule, (v) co-adsorption of CO and O on the metal site, (vi) the transition state (TS2) for $CO + O \rightarrow CO_2$, and (vii) the second produced CO_2.

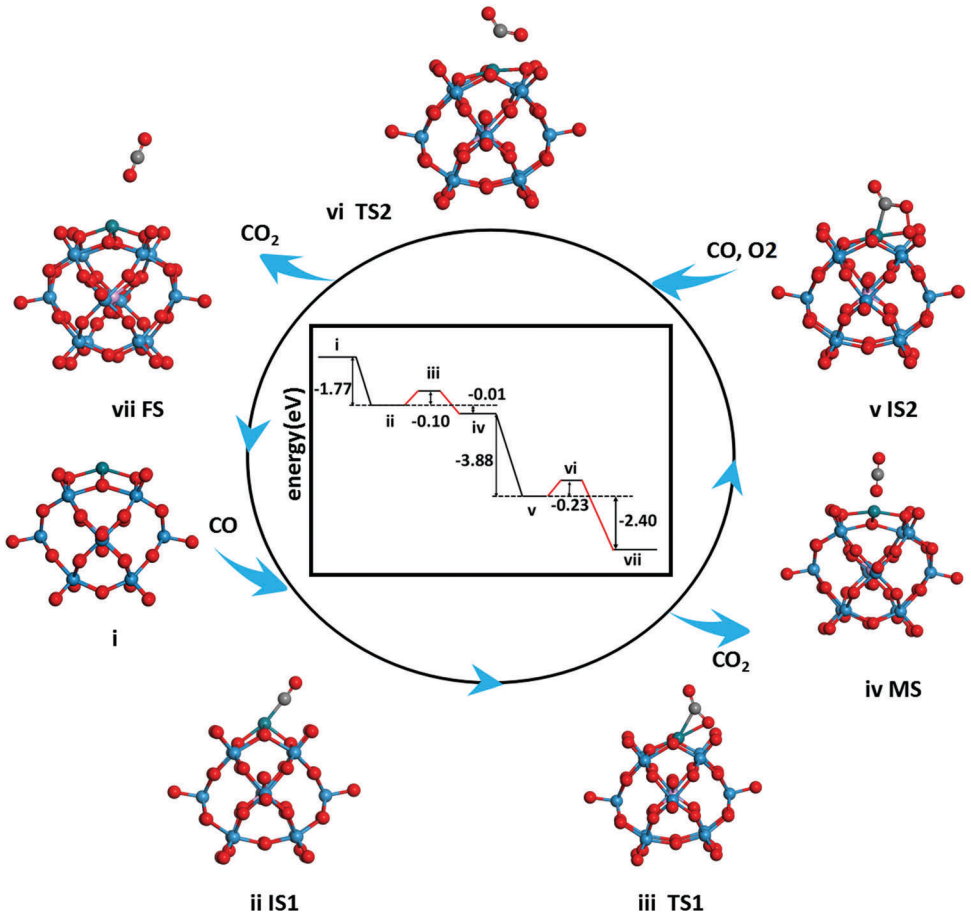

Fig. 6 Diagrams for CO oxidation following the MvK reaction mechanism on PTA supported Rh. (i) Rh-PTA catalyst, (ii) adsorption of CO on the metal site, (iii) the transition state for CO + $O_{lattice}$ → CO_2, (iv) the first produced CO_2 molecule with a generated O vacancy (O_{vac}), (v) co-adsorption of CO and O_2 on Rh and O_{vac} sites, (vi) the transition state (TS2) for CO + O_2 → CO_2 + O_{vac}, (vii) the second produced CO_2 with the catalyst recovered.

While for Rh-PMA and Ru-PMA, the energy barriers (0.87 and 0.75 eV, respectively) for CO oxidation are about ~0.3 eV higher than those (0.53 and 0.47 eV) on Rh_1/FeO_x and $Ru_1/CeO_2(111)$,[24,48] indicating lower activity. It can be also seen that these barriers on M-PMAs (M = Pt, Fe, Ir, Rh, and Ru) are also lower than those of conventional noble metal-based catalysts (~1.0 eV),[49–53] indicating they are potential catalysts for CO oxidation. Free energy pathways for CO oxidation are also calculated (see Fig. S2, ESI†) and the reaction steps that generate CO_2 are in general thermally favored.

In a recent experimental study, Zhang *et al.*[30] proposed that CO oxidation might take place on PTA-supported Rh SACs following the MvK mechanism, in which O atoms are supplied by the catalyst rather than the gas phase. To verify this experimental observation, CI-NEB calculations were performed for CO oxidation on Rh-PTA (see Fig. 6). In the first step, CO reacts with a lattice O atom of PTA to produce CO_2 (CO + $O_{lattice}$ → CO_2), with an energy barrier of 0.10 eV and a small exothermicity of −0.01 eV. Meanwhile, an O vacancy (O_{vac}) is produced. In the second step, an O molecule fills into the O_{vac} site and connects to the Rh atom with a Rh–O bond distance of 1.93 Å and an O–O bond distance of 1.26 Å. The reaction between the second CO species and the adsorbed O_2 to produce CO_2 (CO + O_2 → CO_2 + O_{vac}) has a barrier of 0.23 eV. Such small barriers suggest that the MvK mechanism is a possible mechanism for CO oxidation on Rh-PTA, which is consistent with experimental observations.[30]

To determine whether the MvK mechanism is viable on M-PMA, NEB calculations were performed for CO oxidation on M-PMA following the MvK mechanism. In this case, only Rh-PMA and Fe-PMA are investigated due to the significant computational expense of the NEB calculations. For Rh-PMA, the calculated energy barrier for CO oxidation is approximately 1.38 eV, which is significantly higher than that (0.87 eV) following the LH mechanism. Therefore, the MvK mechanism is less favorable on Rh-PMA. The difference between the values for Rh-PMA and Rh-PTA also suggest that the reaction mechanism might depend on the type of support. For CO oxidation on Fe-PMA, the MvK mechanism is also not preferred because of the energy barrier of 0.97 eV, which is 0.41 eV higher than that of the LH mechanism. These results suggest that the LH mechanism might be the dominant mechanism for CO oxidation over M-PMA.

4. Conclusions

In this work, CO oxidation on PMA-supported single-atom (M = Pt, Au, Co, Cu, Fe, Ir, Ni, Os, Pd, Ag, Rh, or Ru) catalysts

is systematically studied by DFT methods. From electronic structures analysis, it is further confirmed that the metal atoms are very stable at the fourfold oxygen hollow site on PMA. It was found that the adsorbed O_2 molecule can be activated by the single-metal-atom active center supported by PMA since the coupling of the 2p orbitals of O_2 and the 3d orbitals of the metal leads to electron transfer from the M-PMA catalyst to occupy the $2\pi^*$ orbitals of O_2*. CO oxidation on M-PMA following the LH and MvK mechanisms was explored. From the calculation results, it can be seen that the energy barriers are lower than those of conventional noble-metal-based catalysts, indicating they might be potential catalysts for CO oxidation with high activity. In particular, Fe-PMA with the lowest energy barriers for CO oxidation might be a potential non-noble-metal catalyst. The LH mechanism is shown to be more likely for CO oxidation on M-PMA while the MvK mechanism is proved to be unlikely owing to much higher barriers. Further calculations on Rh-PTA indicate that the reaction mechanism might depend on the type of heteropolyacid support.

Conflicts of interest

There are no conflicts to declare.

Acknowledgements

We acknowledge support from National Natural Science Foundation of China (21673040) and Natural Science Foundation of Fujian Province (2016J01052), and Qishan Scholarship Program of Fuzhou University (XRC-17055).

References

1 X. Lei, G. Mbamalu and C. Qin, *J. Phys. Chem. C*, 2017, **121**, 2635–2642.
2 E. H. Song, Z. Wen and Q. Jiang, *J. Phys. Chem. C*, 2011, **115**, 3678–3683.
3 J. S. Elias, N. Artrith, M. Bugnet, L. Giordano, G. A. Botton, A. M. Kolpak and Y. Shao-Horn, *ACS Catal.*, 2016, **6**, 1675–1679.
4 P. Wu, P. Du, H. Zhang and C. Cai, *Phys. Chem. Chem. Phys.*, 2015, **17**, 1441–1449.
5 Z. Wu, D. E. Jiang, A. K. Mann, D. R. Mullins, Z. A. Qiao, L. F. Allard, C. Zeng, R. Jin and S. H. Overbury, *J. Am. Chem. Soc.*, 2014, **136**, 6111–6122.
6 C. Huang, X. Ye, C. Chen, S. Lin and D. Xie, *Comput. Theor. Chem.*, 2013, **1011**, 5–10.
7 H. Y. Kim, H. M. Lee and G. Henkelman, *J. Am. Chem. Soc.*, 2012, **134**, 1560–1570.
8 J. D. Kistler, N. Chotigkrai, P. Xu, B. Enderle, P. Praserthdam, C. Y. Chen, N. D. Browning and B. C. Gates, *Angew. Chem., Int. Ed.*, 2014, **53**, 8904–8907.
9 S. Wang, Y. Feng, M. Yu, Q. Wan and S. Lin, *ACS Appl. Mater. Interfaces*, 2017, **9**, 33267–33273.
10 J. X. Liang, J. Lin, X. F. Yang, A. Q. Wang, B. T. Qiao, J. Liu, T. Zhang and J. Li, *J. Phys. Chem. C*, 2014, **118**, 21945–21951.
11 X. Q. Gong, Z. P. Liu, R. Raval and P. Hu, *J. Am. Chem. Soc.*, 2004, **126**, 8–9.
12 D. Gerçeker and I. Önal, *Appl. Surf. Sci.*, 2013, **285**, 927–936.
13 C. Song, *Catal. Today*, 2002, **77**, 17–49.
14 A. A. Gokhale, J. A. Dumesic and M. Mavrikakis, *J. Am. Chem. Soc.*, 2008, **130**, 1402–1414.
15 M. Gao, A. Lyalin and T. Taketsugu, *J. Chem. Phys.*, 2013, **138**, 034701.
16 M. S. Chen, Y. Cai, Z. Yan, K. K. Gath, S. Axnanda and D. W. Goodman, *Surf. Sci.*, 2007, **601**, 5326–5331.
17 D. Tang and C. Hu, *J. Phys. Chem. Lett.*, 2011, **2**, 2972–2977.
18 W. Zeng, J. Tang, P. Wang and Y. Pei, *RSC Adv.*, 2016, **6**, 55867–55877.
19 M. M. Schubert, S. Hackenberg, A. C. V. Veen, M. Muhler, V. Plzak and R. J. Behm, *J. Catal.*, 2001, **197**, 113–122.
20 B. Qiao, A. Wang, X. Yang, L. F. Allard, Z. Jiang, Y. Cui, J. Liu, J. Li and T. Zhang, *Nat. Chem.*, 2011, **3**, 634–641.
21 X. Zhang, J. Lei, D. Wu, X. Zhao, Y. Jing and Z. Zhou, *J. Mater. Chem. A*, 2016, **4**, 4871–4876.
22 Z. Lu, P. Lv, Z. Yang, S. Li, D. Ma and R. Wu, *Phys. Chem. Chem. Phys.*, 2017, **19**, 16795–16805.
23 G. Pei, X. Liu, A. Wang, A. F. Lee, M. A. Isaacs, L. Li, X. Pan, X. Yang, X. Wang and Z. Tai, *ACS Catal.*, 2015, **5**, 3717–3725.
24 F. Li, Y. Li, X. C. Zeng and Z. Chen, *ACS Catal.*, 2015, **5**, 544–552.
25 Y. Feng, L. Zhou, Q. Wan, S. Lin and H. Guo, *Chem. Sci.*, 2018, **9**, 5890–5896.
26 L. Nie, D. Mei, H. Xiong, B. Peng, Z. Ren, X. Hernandez, A. Delariva, M. Wang, M. H. Engelhard and L. Kovarik, *Science*, 2017, **358**, 1419.
27 H. Wei, X. Liu, A. Wang, L. Zhang, B. Qiao, X. Yang, Y. Huang, M. Shu, J. Liu and T. Zhang, *Nat. Commun.*, 2014, **5**, 5634.
28 J. G. Díaz, Y. Ding, R. Koitz, A. P. Seitsonen, M. Iannuzzi and J. Hutter, *Theor. Chem. Acc.*, 2013, **132**, 1350.
29 B. Zhang, H. Asakura, J. Zhang, J. Zhang, S. De and N. Yan, *Angew. Chem., Int. Ed.*, 2016, **128**, 8319–8323.
30 B. Zhang, H. Asakura and N. Yan, *Ind. Eng. Chem. Res.*, 2017, **56**, 3578–3587.
31 C. G. Liu, M. X. Jiang and Z. M. Su, *Inorg. Chem.*, 2017, **56**, 10496–10504.
32 S. Wang, Y. Feng, S. Lin and H. Guo, *RSC Adv.*, 2017, **7**, 24925–24932.
33 S. Lin, X. Ye, R. S. Johnson and H. Guo, *J. Phys. Chem. C*, 2013, **117**, 17319–17326.
34 C. Jia, G. Zhang, W. Zhong and J. Jiang, *ACS Appl. Mater. Interfaces*, 2016, **8**, 10315–10323.
35 G. Kresse and J. Furthmüller, *Phys. Rev. B*, 1996, **54**, 11169–11186.
36 G. Kresse and J. Hafner, *Phys. Rev. B*, 1993, **47**, 558–561.
37 G. Kresse and J. Furthmüller, *Comput. Mater. Sci.*, 1996, **6**, 15–50.
38 J. P. Perdew and Y. Wang, *Phys. Rev. B*, 1992, **45**, 13244–13249.
39 P. E. Blochl, *Phys. Rev. B*, 1994, **50**, 17953–17979.
40 G. Kresse and D. Joubert, *Phys. Rev. B*, 1999, **59**, 1758–1775.
41 H. J. Monkhorst, *Phys. Rev. B*, 1976, **13**, 5188–5192.

42 G. Henkelman, B. P. Uberuaga and H. Jónsson, *J. Chem. Phys.*, 2000, **113**, 9901–9904.
43 C. D. Zeinalipour, *Surf. Sci.*, 2008, **602**, 1858–1862.
44 C. T. Campbell, G. Ertl, H. Kuipers and J. Segner, *J. Chem. Phys.*, 1980, **73**, 5862–5873.
45 Y. Tang, Y. G. Wang and J. Li, *J. Phys. Chem. C*, 2017, **121**, 11281–11289.
46 C. Wang, X. K. Gu, H. Yan, Y. Lin, J. Li, D. Liu, W. X. Li and J. Lu, *ACS Catal.*, 2017, **7**, 887–891.
47 T. Yang, R. Fukuda, S. Hosokawa, T. Tanaka, S. Sakaki and M. Ehara, *ChemCatChem*, 2017, **9**, 1222–1229.
48 F. Li, L. Li, X. Liu, X. C. Zeng and Z. Chen, *ChemPhysChem*, 2016, **17**, 3170–3175.
49 S. Royer and D. Duprez, *ChemCatChem*, 2011, **3**, 24–65.
50 N. Lopez, T. V. W. Janssens, B. S. Clausen, Y. Xu, M. Mavrikakis, T. Bligaard and J. K. Nørskov, *J. Catal.*, 2004, **223**, 232–235.
51 H. Y. Su, M. M. Yang, X. H. Bao and W. X. Li, *J. Phys. Chem. C*, 2008, **112**, 17303–17310.
52 P. Zhao, Y. Su, Y. Zhang, S. J. Li and G. Chen, *Chem. Phys. Lett.*, 2011, **515**, 159–162.
53 Y. Li, Z. Zhou, G. Yu, W. Chen and Z. Chen, *J. Phys. Chem. C*, 2010, **114**, 6250–6254.

